nature photonics

ARTICLES

https://doi.org/10.1038/s41566-019-0453-z

Experimental realization of a Weyl exceptional ring

Alexander Cerjan[1*], Sheng Huang[2], Mohan Wang[2], Kevin P. Chen[2], Yidong Chong[3,4] and Mikael C. Rechtsman[1]

Weyl points are isolated degeneracies in reciprocal space that are monopoles of the Berry curvature. This topological charge makes them inherently robust to Hermitian perturbations of the system. However, non-Hermitian effects, usually inaccessible in condensed-matter systems, are an important feature of photonic systems, and when added to an otherwise Hermitian Weyl material have been predicted to spread the Berry charge of the Weyl point out onto a ring of exceptional points, creating a Weyl exceptional ring and fundamentally altering its properties. Here, we observe the implications of the Weyl exceptional ring using real-space measurements of an evanescently coupled bipartite optical waveguide array by probing its effects on the Fermi arc surface states and bulk diffraction properties of the two constituent sublattices in an experimental realization of a distributed Berry charge in a topological material.

In recent years, topological phenomena have been extensively explored in both photonics and condensed-matter physics, as these systems can possess exotic states that realize backscattering-immune transport, even in the presence of disorder[1–12]. In three dimensions, perhaps the simplest class of topologically non-trivial systems are Weyl materials[13–28], which possess a set of isolated degeneracies in their band structure that are sources or sinks of Berry curvature[29] and are connected by Fermi arc surface states. As these Weyl points possess a topological charge, they must be created or annihilated in sets of at least two, such that the total charge in the Brillouin zone remains zero. Thus, any isolated Weyl points in a system are protected against Hermitian perturbations that preserve translational symmetry, which can only change their location in the Brillouin zone. Unlike solid-state systems, an important feature of photonic systems is their ability to break Hermiticity through material absorption or gain, as well as radiative outcoupling. This enables photonics to realize phenomena exclusive to non-Hermitian systems, such as exceptional points, a class of degeneracies where two or more eigenvalues and their associated eigenvectors coalesce, and the system possesses a non-trivial Jordan block form[30]. Exceptional points are commonly found in parity–time symmetric systems[31–33] and are associated with a wide range of unusual behaviours in topologically trivial optical systems, such as unconventional reflection and transmission[34,35], promoting single-mode operation in lasers[36,37], novel methods of controlling polarization[38–40] and enhancing the Purcell factor of resonant cavities[41,42].

Despite these successes, only in the last few years have the consequences of non-Hermiticity been explored in topological materials such as topological insulators and Weyl semimetals. There is presently an ongoing theoretical effort to fully classify and characterize such non-Hermitian topological materials, which have been found to exhibit a wide range of unexpected behaviours including anomalous topological winding numbers and breakdowns of bulk-edge correspondence[43–51]. In this context, non-Hermitian Weyl media can serve an exemplary role in understanding the intersection between non-Hermitian and topological materials, because they exhibit a set of distinctive behaviours that have been theoretically predicted[52,53], but have not been previously demonstrated experimentally. In particular, and perhaps surprisingly, adding a non-Hermitian perturbation to a Weyl medium is predicted to expand the Weyl point into a ring of exceptional points—a Weyl exceptional ring (WER)—on which the Berry charge remains real, quantized and equal to the charge of the original Weyl point. As such, WERs are the first known non-point source of Berry flux and cannot be interpreted as magnetic monopoles of the Berry curvature as is standard for Weyl points[52,53]. Because of this, WERs allow for a non-Hermitian topological transition: if the added loss is sufficiently strong, two WERs with opposite charge can merge, annihilating their topological charge to become a single exceptional contour[53].

Here, we experimentally realize a WER in a three-dimensional (3D) photonic lattice composed of evanescently coupled single-mode helical waveguides, fabricated using femtosecond direct laser writing[54]. To confirm that our system possesses a Berry charge, we first show that our waveguide array exhibits a topological transition beyond which we observe protected surface states. We then show that this transition is an exemplar of a new class of topological transitions, where the upper and lower bands meet at a ring, rather than a point, by observing the lack of conical diffraction at this transition when the system is non-Hermitian. Taken together, these measurements demonstrate that we have realized a ring-like object in the reciprocal space of our system with quantized Berry charge—that is, a WER.

Our experimental system consists of a bipartite array of helical waveguides with the same orientation, which breaks the parity symmetry of the system and allows for the formation of Weyl points or WERs. To remove the Hermiticity of this system, breaks are inserted into one of the two sublattices by periodically skipping the writing of a specified length of these waveguides, as shown in Fig. 1a–c (see Methods). Within these breaks the confining potential for the light is removed, resulting in strong coupling to radiating modes and yielding a tunable mechanism for adding loss by increasing the length of these breaks (Supplementary Fig. 1). Thus, by starting with the paraxial wave equation for weakly confined waveguide modes, we show that the 3D band structure of this system realizes the 2×2 non-Hermitian Weyl exceptional ring Hamiltonian:

$$\hat{H} \approx v_{\perp}(\delta k_x \hat{\sigma}_x + \delta k_y \hat{\sigma}_y) + v_z \delta k_z (\hat{I} - |b|\hat{\sigma}_z) - i v_z \tau (\hat{\sigma}_z + \hat{I}) \quad (1)$$

[1]Department of Physics, The Pennsylvania State University, University Park, PA, USA. [2]Department of Electrical and Computer Engineering, University of Pittsburgh, Pittsburgh, PA, USA. [3]School of Physical and Mathematical Sciences, Nanyang Technological University, Singapore, Singapore. [4]Centre for Disruptive Photonic Technologies, Nanyang Technological University, Singapore, Singapore. *e-mail: awc19@psu.edu

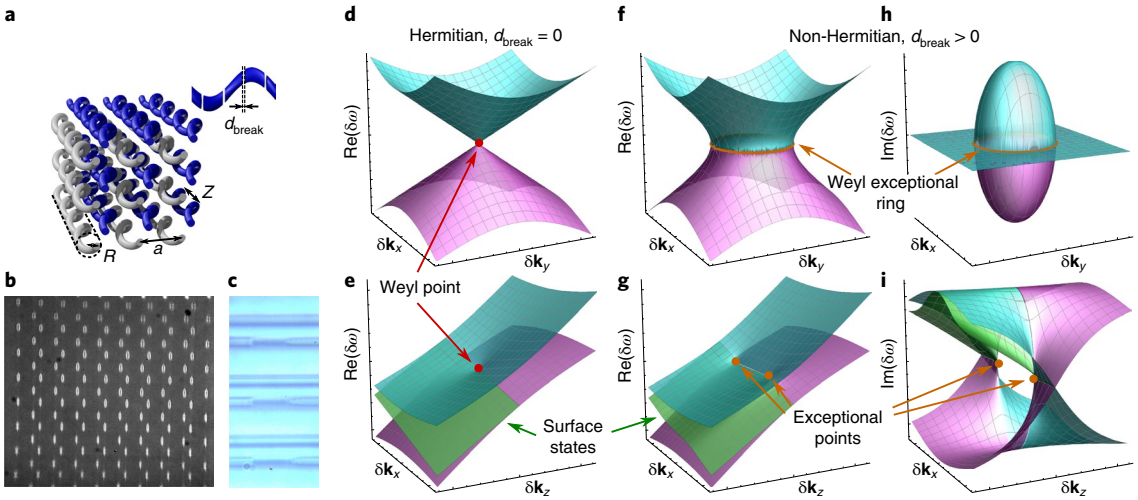

Fig. 1 | Helical waveguide array and corresponding band structure supporting a WER. a, Schematic of the bipartite helical waveguide array in which all of the helices have the same orientation, but the rotations of the two sublattices are a half-cycle out of phase and breaks have been added to one of the sublattices. In this system $R = 4\,\mu m$, $a = 29\sqrt{2}\,\mu m$, $Z = 1\,cm$ and 16 evenly spaced breaks with length d_{break} are added per helix period Z. **b**, Greyscale microscope image of the output facet of one of the helical waveguide arrays. **c**, Microscope image showing breaks added to the top layer of a helical waveguide array. Within the breaks, out-of-focus waveguides deeper in the array can be seen. **d**,**e**, Band structures in the δk_x–δk_y and δk_x–δk_z planes with $\delta k_y = 0$ and $\delta k_z = 0$, respectively, for a Hermitian waveguide array, $\tau = 0$, showing a type-II Weyl point, marked in red. **f**,**g**, Similar to **d** and **e**, except with breaks added to the waveguides, $\tau = 0.2$, so that the band structure possesses a WER in the δk_x–δk_y plane that is intersected twice by the δk_x–δk_z plane, exhibiting two exceptional points, marked in orange. **h**,**i**, Imaginary part of the band structure for the same systems considered in **f** and **g**. Surface states are shown schematically in green in **e**, **g** and **i** for the states localized to the surface with unbroken waveguides.

whose eigenvalues, $\delta\omega$, are the band frequencies relative to the frequency of the underlying Weyl point for the wavevector components perpendicular, $\delta\mathbf{k}_\perp = (\delta k_x, \delta k_y)$, and parallel, δk_z, to the waveguide axis. The details of this derivation are included in the Supplementary Information. Here, τ characterizes the strength of the loss added to one of the two sublattices of waveguides, $v_\perp$ and v_z are the group velocities in the transverse and parallel directions, respectively, $\hat{\sigma}_{x,y,z}$ are the Pauli matrices, $\hat{I}$ is the identity and b is a dimensionless parameter, with $|b| \ll 1$.

In the Hermitian limit, $\tau = 0$, this helical waveguide array possesses a type-II Weyl point, whose dispersion is strongly anisotropic because both bands represent modes travelling in the same direction along the z axis[27]. Here we consider the helical waveguide array as a 3D photonic crystal, rather than a 2D system in the paraxial limit, where a Weyl point exists in the $\delta\omega(k_x, k_y, k_z)$ band structure. Although there is a complementary pair of bands representing modes travelling in the opposite direction at the same frequency, the weak backscattering in this system implies negligible coupling between the forward and backward propagating modes, allowing either pair of bands to be considered independent of the other. The distinctive conical band structure of this system at the Weyl point, $\delta\omega = 0$, is shown in Fig. 1d,e, yielding a constant transverse group velocity at this frequency across nearly the entire transverse Brillouin zone.

However, as loss is added to one sublattice in the bipartite waveguide array by increasing the break lengths, $|\tau| > 0$, the two bands begin to merge together starting at the Weyl point, and proceeding radially outward in the transverse direction, as shown in Fig. 1f,h. This process yields a 1D closed contour of exceptional points in the $\delta k_z = 0$ plane where the upper and lower bands merge together and on which the Berry charge of the underlying Weyl point is exactly preserved, forming a WER[52,53]. Within this circular region in $\delta\mathbf{k}_\perp$, and for a range of δk_z near that of the WER, the real part of the bands are nearly flat, resulting in an extremely small transverse intensity transport velocity, which is the non-Hermitian generalization of the group velocity we observe in waveguide arrays[55]. These flat bands can be seen by viewing the band structure in the $\delta k_x - \delta k_z$ plane, shown in Fig. 1g,i for $\delta k_y = 0$, between the two exceptional points where this plane intersects the WER.

Although the spatial distribution of loss in this system resembles that of parity–time symmetric systems[33–35], the presence of the helices also breaks the parity symmetry of the system, and overall, the system is not parity–time symmetric. Furthermore, to form a WER, it is critical that the loss is only added to a single sublattice of the system, which realizes the non-trivial non-Hermitian term $iv_z\tau\hat{\sigma}_z$ in equation (1). Adding an equal amount of loss to both sublattices would represent a trivial non-Hermitian perturbation of the form $iv_z\tau\hat{I}$, which preserves the Weyl point, as shown in the Supplementary Information. Finally, as the refractive index within the waveguides only differs from the surrounding glass by $\Delta n = 2.6 \times 10^{-3}$, Fresnel reflection at the waveguide break interfaces can be ignored, as also discussed in the Supplementary Information.

One important consequence of the presence of quantized sources or sinks of Berry flux in the spectrum of a system is the appearance of Fermi arc surface states at the spatial boundaries of the device. In a Hermitian system, these surface states form open arcs connecting the projections of pairs of Weyl points with opposite Berry charge in the surface Brillouin zone, as shown in Fig. 2a. When the system becomes non-Hermitian, the Fermi arc states persist, but now connect the projection of the pair of WERs that formed from the underlying Weyl points, as shown in Fig. 2b.

Given the large disparity between their transverse and longitudinal lattice constants, helical waveguide arrays are typically analysed in the paraxial limit to separate these two scales[56]. Then, Maxwell's equations describing light diffracting through the waveguide array can be approximated as a 2D Schrödinger-like equation, in which z acts as a temporal direction, and the potential confining the light is proportional to the index of refraction of the waveguides relative to the surrounding index, $\Delta n(x, y, z)$. Using this paraxial approximation, the operating frequency becomes an adjustable parameter

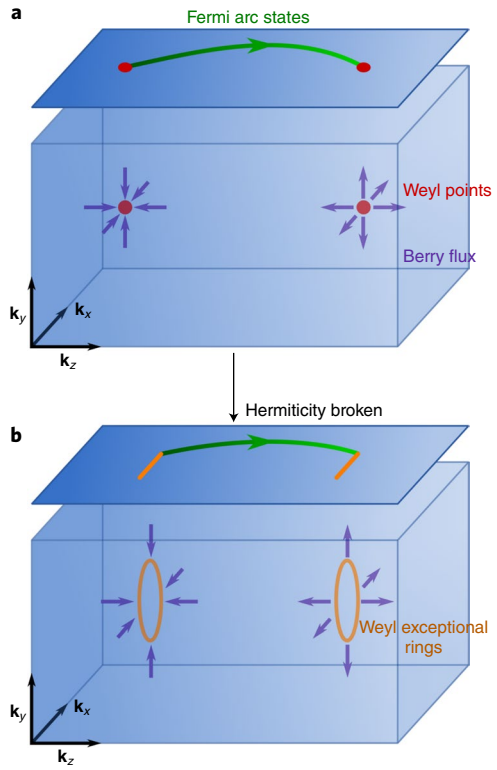

Fig. 2 | Surface states connecting the projection of the Berry charges. **a**, Schematic of the Fermi arc surface states (green) connecting the projections of the two Weyl points (red) in the Hermitian bipartite helical waveguide array. Berry flux is shown in purple. **b**, Similar to **a** except with loss added to one sublattice of the system, such that the Fermi arc surface states now connect the projections of the WERs (orange).

while the longitudinal wavevector component, k_z, acts as an effective 'energy', and thus solutions to these equations yield isofrequency surfaces of the full 3D band structure. For non-Hermitian paraxial systems, the amplification or attenuation of a band is instead found as the imaginary part of k_z, yielding gain or loss per unit length in z. As our system contains a Weyl point or WER at $\delta\omega = 0$, different choices of frequency can result in topologically distinct 2D band structures of the paraxial equation. In particular, isofrequency surfaces for $\delta\omega > 0$ are conventional insulators (in the sense that they have a topologically trivial bandgap), while those for $\delta\omega < 0$ are topological insulators.

To experimentally demonstrate that this helical waveguide array possesses a WER, we observe the real-space behaviours associated with its presence in the system's band structure. First, to show that our system possesses a Berry charge, we demonstrate that our system exhibits a topological transition by observing the appearance of Fermi arc surface states for increasing d_{break}. Second, to show that this Berry charge is distributed along a ring rather than condensed at a point, we demonstrate that a signal injected into the centre of the waveguide array at the topological transition experiences progressively more localization for increasing d_{break} due to the expansion of the radius of the flat band region within the WER. A final check that our system correctly realizes the $iv_z\tau\hat{\sigma}_z$ term in equation (1) is presented in the Supplementary Information, where we observe the ratio of the output power carried in the two sublattices of the system to demonstrate the collapse of the eigenmodes into different sublattices due to the non-uniform distribution of the loss.

The observation of a topological transition in this helical waveguide array relies on an additional consequence of creating loss in the system by adding breaks to the waveguides: light propagating within a break in the lossy waveguide accumulates phase at a slower rate than light propagating in the lossless waveguide due to the lower index of refraction in these breaks relative to the index of an unbroken waveguide. As we show in the Supplementary Information, this difference in phase accumulation adds an additional term proportional to $\hat{\sigma}_z$ to equation (1) that decreases the wavelength where the topological transition due to the Weyl point or WER occurs. Thus, by fixing the operating wavelength and increasing the break length, the chosen isofrequency surface can be driven through a topological transition due to the motion of the WER. To observe this topological transition, we inject light into a single waveguide at the boundary of the lattice and look for the appearance of Fermi arc surface states at the output facet of the system. If a surface state is present, light should remain relatively confined to the system's surface, otherwise it will diffract into the bulk. The wavelength is fixed at $\lambda = 1{,}580$ nm, which is less than the wavelength of the Weyl point in the Hermitian system when $d_{\mathrm{break}} = 0\,\mu$m, at $\lambda_{\mathrm{WP}} = 1{,}609$ nm. Thus, at this wavelength the injected signal in the Hermitian system simply diffracts, as there is no Fermi arc state at the operating wavelength, shown in Fig. 3a. However, as d_{break} is increased as shown in Fig. 3b,c, the wavelength of the topological transition at the WER decreases, leading to the appearance of a Fermi arc surface state for $d_{\mathrm{break}} = 60\,\mu$m, as shown in Fig. 3d. Simulations confirm the appearance of Fermi arc surface states as shown in Fig. 3e–l. At $d_{\mathrm{break}} = 60\,\mu$m, simulations predict that the WER is at $\lambda_{\mathrm{WER}} = 1{,}480$ nm. Thus, our system realizes a topological transition beyond which protected surface states appear, demonstrating that the system possesses a Berry charge.

To demonstrate that the topological transition in the previous experiment is due to a WER and not a Weyl point, we studied the consequences of opening a flat band region at the centre of the Brillouin zone. As the underlying Hermitian system with $d_{\mathrm{break}} = 0\,\mu$m possesses a type-II Weyl point, its isofrequency surface at this point is conical, leading to a large transverse group velocity, as shown in Fig. 4e. However, for either shorter or longer wavelengths the isofrequency surfaces are hyperbolic. Thus, when light is injected into the centre of the structure for propagation distances in z short enough that the beam does not reflect off the boundary of the system, the Weyl point is seen as a peak in the transverse radial expectation value, $\langle\psi|\mathbf{r}_\perp|\psi\rangle/a$. In the cyan curve of Fig. 4a,b, which corresponds to the Hermitian waveguide array, the peak of the experimentally observed transverse radial expectation value is in close agreement with the numerically predicted location of the Weyl point at $\lambda = 1{,}609$ nm. However, as the waveguide break length is increased, shifting the location of the topological transition to shorter wavelengths, the peak in the transverse radial expectation value disappears and $\langle\psi|\mathbf{r}_\perp|\psi\rangle/a$ is reduced over the entire measured wavelength range when compared with the lossless system, indicating that there is no significant difference in this quantity between wavelengths where the topological transition occurs and wavelengths with hyperbolic dispersion, shown in increasingly more magenta colours in Fig. 4a,b. The output intensity in the waveguide array along with simulated isofrequency surfaces at the Weyl point of the Hermitian system and at the WER when $d_{\mathrm{break}} = 60\,\mu$m are shown in Fig. 4c–h. This observation is consistent with the formation of a WER in the helical waveguide array, and inconsistent with the existence of an ordinary Weyl point, as a WER flattens the centre of the isofrequency surface in the Brillouin zone and decreases the transverse intensity transport velocity. Thus, this experiment demonstrates that the system experiences a topological transition without a conventional band touching at a Weyl point, and as such is unlike any previously observed topological transition.

In conclusion, we have observed a helical waveguide array supporting a WER in the optical regime by adding breaks to half of the waveguides, breaking the Hermiticity of the system. As we have shown, non-Hermitian perturbations to a Weyl material yield a

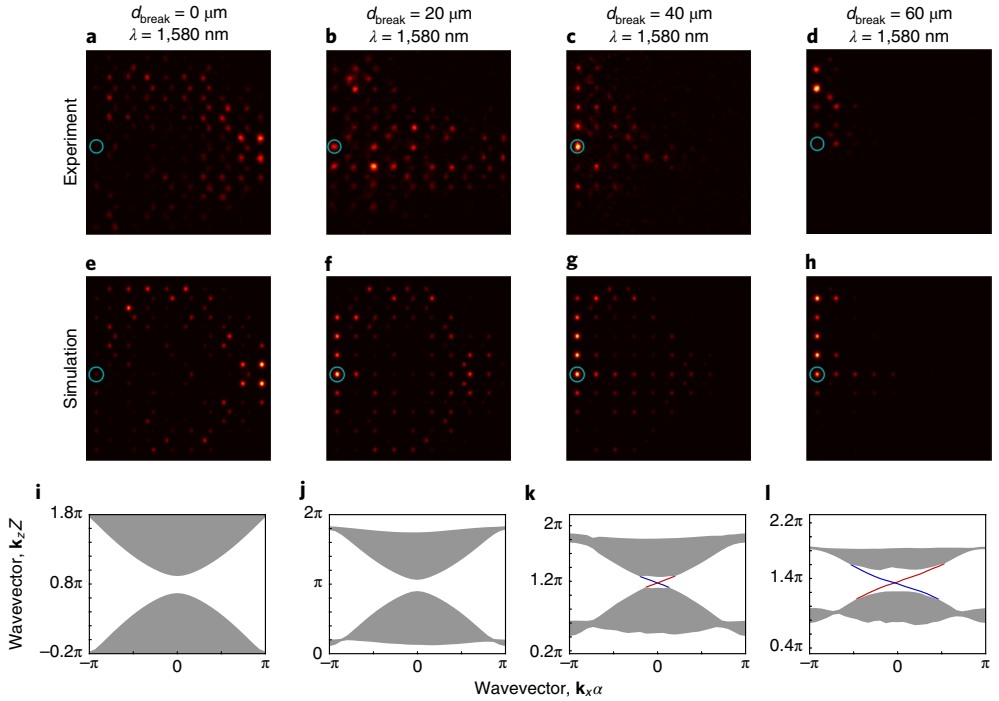

Fig. 3 | Direct observation of a topological transition through the emergence of Fermi arc surface states. a–d, Output intensity plots when light is injected into a single waveguide at the centre-left of the lattice, indicated by cyan circle, with a total system length of $L = 8$ cm, at $\lambda = 1{,}580$ nm, for four different break lengths, $d_{break} = 0$, 20, 40, 60 μm. This drives the system through a topological transition, and a Fermi arc state is seen in **d**. **e–h**, Corresponding full-wave simulation results calculated using the beam propagation method, showing good agreement with the experimental results. **i–l**, Isofrequency surface projections of a semi-infinite helical waveguide array calculated using full-wave simulations and a diagonalization procedure[57]. Blue and red curves denote surface states travelling on the left and right of the device, while grey indicates the bulk bands.

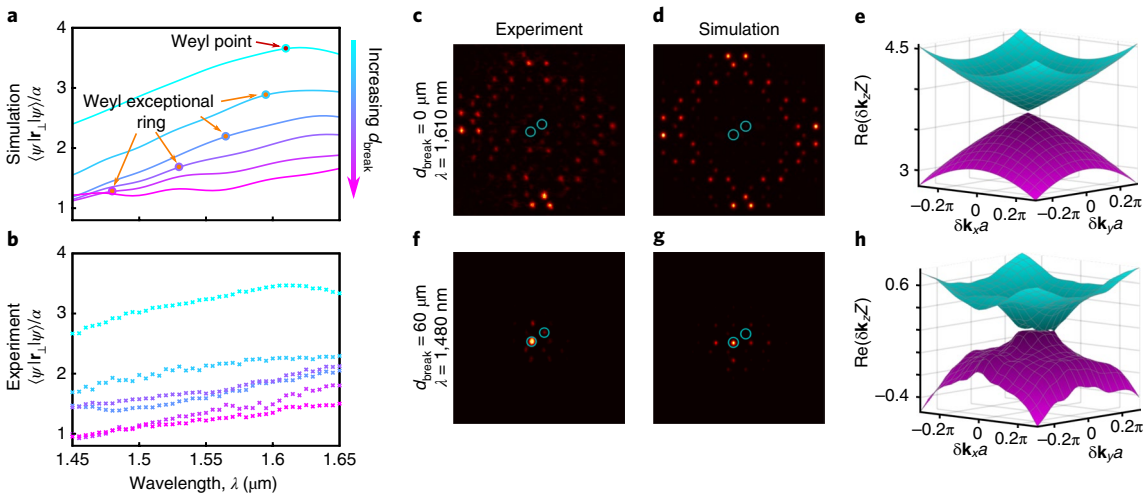

Fig. 4 | Distinguishing a WER from a Weyl point by observing the transverse radial propagation. a,**b**, Simulations and experimental observations of the transverse radial propagation, $\langle\psi|\mathbf{r}_\perp|\psi\rangle/a$, for light injected into the centre of the helical waveguide array as a function of the injected wavelength for six different break lengths $d_{break} = 0$, 20, 40, 50, 60, 70 μm. The Hermitian system is shown in cyan, and increasingly magenta colours indicate longer break lengths. Wavelengths where simulations predict either a Weyl point or WER are indicated in red and orange, respectively. (For $d_{break} = 70$ μm the transition occurs near $\lambda = 1{,}400$ nm.) **c**,**d**, Output intensity plots for light injected into the centre of the system at the two indicated waveguides for the Hermitian system at the topological transition, $\lambda_{WP} = 1{,}609$ nm, with a system length of $L = 4$ cm. **e**, Isofrequency surface for the Hermitian system at the topological transition calculated using full-wave simulations and a diagonalization procedure[57]. **f–h**, Similar to **c–e**, except for the non-Hermitian system with $d_{break} = 60$ μm at $\lambda = 1{,}480$ nm. Note that the roughness seen in the non-Hermitian band structure simulations in **h** is a numerical artefact in the diagonalization procedure stemming from the large radiative background when $d_{break} > 0$ μm.

fundamentally new class of topological object, WERs. This experiment not only provides the first observation of a distributed source of Berry flux, but also directly demonstrates that Berry charge and Fermi arc surface states are preserved in the presence of a non-Hermitian perturbation to the system, even as the Weyl point itself transforms into a WER. This experimental demonstration of analytic predictions of the properties of non-Hermitian Weyl materials provides strong motivation for additional theoretical and experimental studies, in particular those exploring the complex interplay between band topology and the non-trivial topological structure associated with exceptional points, as well as the ramifications of distributed sources of Berry flux. The fact that WERs can merge to realize a topological phase transition dependent only on the strength of the non-Hermiticity allows for a new route to obtaining tunable photonic topological materials[53]. Likewise, as point degeneracies, Weyl points are the most natural places to nucleate WERs in 3D photonic crystals and explore the novel interplay between exceptional point physics and Purcell enhancement[41,42].

Online content

Any methods, additional references, Nature Research reporting summaries, source data, statements of code and data availability and associated accession codes are available at https://doi.org/10.1038/s41566-019-0453-z.

Received: 8 March 2019; Accepted: 29 April 2019;
Published online: 17 June 2019

References

1. Hasan, M. Z. & Kane, C. L. Colloquium: topological insulators. *Rev. Mod. Phys.* **82**, 3045–3067 (2010).
2. Ozawa, T. et al. Topological photonics. *Rev. Mod. Phys.* **91**, 015006 (2019).
3. Haldane, F. D. M. & Raghu, S. Possible realization of directional optical waveguides in photonic crystals with broken time-reversal symmetry. *Phys. Rev. Lett.* **100**, 013904 (2008).
4. Wang, Z., Chong, Y., Joannopoulos, J. D. & Soljačić, M. Observation of unidirectional backscattering-immune topological electromagnetic states. *Nature* **461**, 772–775 (2009).
5. Umucallar, R. O. & Carusotto, I. Artificial gauge field for photons in coupled cavity arrays. *Phys. Rev. A* **84**, 043804 (2011).
6. Hafezi, M., Demler, E. A., Lukin, M. D. & Taylor, J. M. Robust optical delay lines with topological protection. *Nat. Phys.* **7**, 907–912 (2011).
7. Fang, K., Yu, Z. & Fan, S. Realizing effective magnetic field for photons by controlling the phase of dynamic modulation. *Nat. Photon.* **6**, 782–787 (2012).
8. Kraus, Y. E., Lahini, Y., Ringel, Z., Verbin, M. & Zilberberg, O. Topological states and adiabatic pumping in quasicrystals. *Phys. Rev. Lett.* **109**, 106402 (2012).
9. Kitagawa, T. et al. Observation of topologically protected bound states in photonic quantum walks. *Nat. Commun.* **3**, 1872 (2012).
10. Rechtsman, M. C. et al. Photonic Floquet topological insulators. *Nature* **496**, 196–200 (2013).
11. Khanikaev, A. B. et al. Photonic topological insulators. *Nat. Mater.* **12**, 233–239 (2013).
12. Hafezi, M., Mittal, S., Fan, J., Migdall, A. & Taylor, J. M. Imaging topological edge states in silicon photonics. *Nat. Photon.* **7**, 1001–1005 (2013).
13. Wan, X., Turner, A. M., Vishwanath, A. & Savrasov, S. Y. Topological semimetal and Fermi-arc surface states in the electronic structure of pyrochlore iridates. *Phys. Rev. B* **83**, 205101 (2011).
14. Yang, K.-Y., Lu, Y.-M. & Ran, Y. Quantum Hall effects in a Weyl semimetal: possible application in pyrochlore iridates. *Phys. Rev. B* **84**, 075129 (2011).
15. Lu, L., Fu, L., Joannopoulos, J. D. & Soljačić, M. Weyl points and line nodes in gyroid photonic crystals. *Nat. Photon.* **7**, 294–299 (2013).
16. Xu, S.-Y. et al. Discovery of a Weyl fermion semimetal and topological Fermi arcs. *Science* **349**, 613–617 (2015).
17. Lu, L. et al. Experimental observation of Weyl points. *Science* **349**, 622–624 (2015).
18. Lv, B. Q. et al. Observation of Weyl nodes in TaAs. *Nat. Phys.* **11**, 724–727 (2015).
19. Yang, L. X. et al. Weyl semimetal phase in the non-centrosymmetric compound TaAs. *Nat. Phys.* **11**, 728–732 (2015).
20. Soluyanov, A. A. et al. Type-II Weyl semimetals. *Nature* **527**, 495–498 (2015).
21. Xiao, M., Chen, W.-J., He, W.-Y. & Chan, C. T. Synthetic gauge flux and Weyl points in acoustic systems. *Nat. Phys.* **11**, 920–924 (2015).
22. Chen, W.-J., Xiao, M. & Chan, C. T. Photonic crystals possessing multiple Weyl points and the experimental observation of robust surface states. *Nat. Commun.* **7**, 13038 (2016).
23. Lin, Q., Xiao, M., Yuan, L. & Fan, S. Photonic Weyl point in a two-dimensional resonator lattice with a synthetic frequency dimension. *Nat. Commun.* **7**, 13731 (2016).
24. Xiao, M., Lin, Q. & Fan, S. Hyperbolic Weyl point in reciprocal chiral metamaterials. *Phys. Rev. Lett.* **117**, 057401 (2016).
25. Gao, W. et al. Photonic Weyl degeneracies in magnetized plasma. *Nat. Commun.* **7**, 12435 (2016).
26. Fang, C., Lu, L., Liu, J. & Fu, L. Topological semimetals with helicoid surface states. *Nat. Phys.* **12**, 936–941 (2016).
27. Noh, J. et al. Experimental observation of optical Weyl points and Fermi arc-like surface states. *Nat. Phys.* **13**, 611 (2017).
28. Goi, E., Yue, Z., Cumming, B. P. & Gu, M. Observation of type I photonic Weyl points in optical frequencies. *Laser Photonics Rev.* **12**, 1700271 (2018).
29. Berry, M. V. Quantal phase factors accompanying adiabatic changes. *Proc. R. Soc. Lond. A* **392**, 45–57 (1984).
30. Kato, T. *Perturbation Theory for Linear Operators* 2nd edn (Springer, 1995).
31. Bender, C. M., Boettcher, S. & Meisinger, P. N. PT-symmetric quantum mechanics. *J. Math. Phys.* **40**, 2201–2229 (1999).
32. Bender, C. M., Brody, D. C. & Jones, H. F. Complex extension of quantum mechanics. *Phys. Rev. Lett.* **89**, 270401 (2002).
33. Makris, K. G., El-Ganainy, R., Christodoulides, D. N. & Musslimani, Z. H. Beam dynamics in PT symmetric optical lattices. *Phys. Rev. Lett.* **100**, 103904 (2008).
34. Lin, Z. et al. Unidirectional invisibility induced by PT-symmetric periodic structures. *Phys. Rev. Lett.* **106**, 213901 (2011).
35. Peng, B. et al. Parity-time-symmetric whispering-gallery microcavities. *Nat. Phys.* **10**, 394–398 (2014).
36. Hodaei, H., Miri, M.-A., Heinrich, M., Christodoulides, D. N. & Khajavikhan, M. Parity-time-symmetric microring lasers. *Science* **346**, 975–978 (2014).
37. Feng, L., Wong, Z. J., Ma, R.-M., Wang, Y. & Zhang, X. Single-mode laser by parity-time symmetry breaking. *Science* **346**, 972–975 (2014).
38. Lawrence, M. et al. Manifestation of PT symmetry breaking in polarization space with terahertz metasurfaces. *Phys. Rev. Lett.* **113**, 093901 (2014).
39. Cerjan, A. & Fan, S. Achieving arbitrary control over pairs of polarization states using complex birefringent metamaterials. *Phys. Rev. Lett.* **118**, 253902 (2017).
40. Zhou, H. et al. Observation of bulk Fermi arc and polarization half charge from paired exceptional points. *Science* **359**, 1009–1012 (2018).
41. Lin, Z., Pick, A., Lončar, M. & Rodriguez, A. W. Enhanced spontaneous emission at third-order Dirac exceptional points in inverse-designed photonic crystals. *Phys. Rev. Lett.* **117**, 107402 (2016).
42. Pick, A., Lin, Z., Jin, W. & Rodriguez, A. W. Enhanced nonlinear frequency conversion and Purcell enhancement at exceptional points. *Phys. Rev. B* **96**, 224303 (2017).
43. Zeuner, J. M. et al. Observation of a topological transition in the bulk of a non-Hermitian system. *Phys. Rev. Lett.* **115**, 040402 (2015).
44. Lee, T. E. Anomalous edge state in a non-Hermitian lattice. *Phys. Rev. Lett.* **116**, 133903 (2016).
45. Leykam, D., Bliokh, K. Y., Huang, C., Chong, Y. & Nori, F. Edge modes, degeneracies, and topological numbers in non-Hermitian systems. *Phys. Rev. Lett.* **118**, 040401 (2017).
46. Weimann, S. et al. Topologically protected bound states in photonic parity-time-symmetric crystals. *Nat. Mater.* **16**, 433–438 (2017).
47. Shen, H., Zhen, B. & Fu, L. Topological band theory for non-Hermitian hamiltonians. *Phys. Rev. Lett.* **120**, 146402 (2018).
48. Kunst, F. K., Edvardsson, E., Budich, J. C. & Bergholtz, E. J. Biorthogonal bulk-boundary correspondence in non-Hermitian systems. *Phys. Rev. Lett.* **121**, 026808 (2018).
49. Yao, S. & Wang, Z. Edge states and topological invariants of non-Hermitian systems. *Phys. Rev. Lett.* **121**, 086803 (2018).
50. Gong, Z. et al. Topological phases of non-Hermitian systems. *Phys. Rev. X* **8**, 031079 (2018).
51. Kremer, M. et al. Demonstration of a two-dimensional PT-symmetric crystal. *Nat. Commun.* **10**, 435 (2019).
52. Xu, Y., Wang, S.-T. & Duan, L.-M. Weyl exceptional rings in a three-dimensional dissipative cold atomic gas. *Phys. Rev. Lett.* **118**, 045701 (2017).
53. Cerjan, A., Xiao, M., Yuan, L. & Fan, S. Effects of non-Hermitian perturbations on Weyl hamiltonians with arbitrary topological charges. *Phys. Rev. B* **97**, 075128 (2018).
54. Szameit, A. & Nolte, S. Discrete optics in femtosecond-laser-written photonic structures. *J. Phys. B* **43**, 163001 (2010).
55. Schomerus, H. & Wiersig, J. Non-Hermitian-transport effects in coupled-resonator optical waveguides. *Phys. Rev. A* **90**, 053819 (2014).

56. Yariv, A. & Yeh, P. *Optical Waves in Crystals: Propagation and Control of Laser Radiation* (Wiley, 1984).
57. Leykam, D., Rechtsman, M. & Chong, Y. Anomalous topological phases and unpaired Dirac cones in photonic floquet topological insulators. *Phys. Rev. Lett.* **117**, 013902 (2016).

Acknowledgements

The authors thank J. Noh for discussions about experimental techniques. M.C.R. and A.C. acknowledge support from the National Science Foundation under grants ECCS-1509546 and DMS-1620422 as well as the Packard Foundation via fellowship no. 2017-66821, and the Charles E. Kaufman foundation under grant no. KA2017-91788. K.P.C., S.H. and M.W. acknowledge National Science Foundation grants ECCS-1509199 and DMS-1620218. Y.D.C. is supported by Singapore MOE Academic Research Fund Tier 2 Grants MOE2015-T2-2-008 and MOE2016-T2-1-128, and Singapore MOE Academic Research Fund Tier 3 Grant MOE2016-T3-1-006.

Author contributions

A.C. conceived of the idea, carried out the experimental measurements, and performed the data analysis and numerical simulations. A.C. and M.C.R. designed the experiments. A.C., Y.D.C. and M.C.R. performed the theoretical analysis and wrote the manuscript. S.H. and M.W. developed the laser fabrication process and characterized the samples under the supervision of K.P.C. The project was supervised by M.C.R. All authors contributed to discussions and to finalizing the manuscript.

Competing interests

The authors declare no competing interests.

Additional information

Supplementary information is available for this paper at https://doi.org/10.1038/s41566-019-0453-z.

Reprints and permissions information is available at www.nature.com/reprints.

Correspondence and requests for materials should be addressed to A.C.

Publisher's note: Springer Nature remains neutral with regard to jurisdictional claims in published maps and institutional affiliations.

Methods

The helical waveguide arrays were written, using a Ti:sapphire laser and amplifier system (Coherent:RegA 9000; repetition rate of 250 kHz, pulse duration of 270 fs and pulse energy of 880 nJ), into Corning Eagle XG borosilicate glass with an index of refraction of $n_0 = 1.473$. The size and shape of the focal volume within the glass chip of the laser writing beam were specified by first sending the laser through a beam-shaping cylindrical telescope and then focusing it using a ×50, aberration-corrected microscope objective (NA = 0.55). The waveguides were then fabricated by translating the glass chip through the laser's focal volume using a high-precision three-axis Aerotech motion stage (model ABL20020). The breaks in the waveguide were created by turning off the laser writing beam using an acousto-optical modulator while the motion stage continued to move, and then turning the beam back on after the desired distance was reached.

To perform the experiments reported in the main text, light was injected into the helical waveguide arrays at the input facet of the system by butt-coupling a single-mode optical fibre to a single waveguide, which in turn was coupled to the full waveguide array. A tunable, 1,450–1,650 nm, mid-infrared diode laser (Agilent 8164B) was used as the input light source. After propagating through the array, light from the output facet of the glass chip was collected using a 0.2 NA microscope objective lens and observed using a near-infrared InGaAs camera (ICI systems).

Data availability

The data that support the findings of this study are available from the corresponding author on reasonable request.

Code availability

The code used in this study is available from the corresponding author on reasonable request.